

# Superconductivity in imbalanced bilayer Hubbard model: enhanced $d$ -wave and weakened $s^\pm$ -wave pairing

Ziying Jia,<sup>1</sup> Xun Liu,<sup>1</sup> and Mi Jiang<sup>1,2</sup>

<sup>1</sup>*School of Physical Science and Technology, Soochow University, Suzhou 215006, China*

<sup>2</sup>*Jiangsu Key Laboratory of Frontier Material Physics and Devices, Soochow University, Suzhou 215006, China*

We investigate the bilayer model with two layers of imbalanced densities coupled by the interlayer hybridization. Using the large-scale dynamical cluster quantum Monte Carlo simulation, we discovered that increased hybridization induces a transition in the superconducting pairing from  $d$ -wave to  $s^\pm$ -wave and the superconducting  $T_c$  of  $d$ -wave pairing exhibits a non-monotonic dependence on the density imbalance. Remarkably, the optimal SC occurs at a moderate imbalance, whose SC is solely hosted by the layer with higher density (lower hole doping). Our results support the possibility of  $T_c$  enhancement in composite picture where the underdoped layer provides the pairing strength while the overdoped layer promotes the phase coherence. The uncovered SC hosted by a single layer is reminiscent of our recent exploration on the trilayer Hubbard model. Our present study thus provides new insight that the SC can be enhanced via the layer differentiation.

## I. INTRODUCTION

The two-dimensional bilayer Hubbard model has been extensively investigated for their superconductivity (SC), exciton condensation, magnetic properties etc. [1–7]. Early studies revealed the regulatory effect of charge imbalance on interlayer magnetic coupling [8]. The phase transition between antiferromagnetic and band insulator has also been systematically studied by quantum Monte Carlo (QMC) and other advanced many-body methods[9, 10]. With the discovery of high-temperature SC in nickelates[11], the current research focuses on various pairing instabilities and mechanism in the two-orbital bilayer model[12–24]. Besides, electron-hole pairs and exciton condensation in bilayer system with tunable interlayer attraction or repulsion is also a widely studied problem[6, 25–27].

In high-temperature superconductors, the interlayer coupling in bilayer systems is crucial for the pairing symmetry. Previous studies have demonstrated that weakly coupled bilayer systems exhibit  $d$ -wave pairing [1–3]; while stronger interlayer coupling induces a transition from  $d$ -wave to  $s^\pm$ -wave pairing [28, 29], along with the emergence of additional phases such as the pseudogap [30]. Recent studies have revealed competition between  $d$  and  $d+is$  pairing in two-dimensional lattice models[31], which is governed by carrier density and intralayer hopping. The bilayer systems exhibit similar complexity and early studies demonstrated that “critical” interlayer hopping could potentially stabilize the  $d+is$  pairing symmetry[28]. Notably, ultracold atomic experiments observing competing magnetic orders [4, 32], non-local density fluctuation [33] and superfluid [34] confirmed that the bilayer model has tangible physical relevance.

Apart from the standard situation with two equivalent layers, the bilayer systems with two imbalanced layers are of interest as well. For example, the composite picture provides the possibility that an underdoped layer (UL) enhances the pairing scale while the other optimally or overdoped layer (OL) supplies phase stiffness [35, 36].

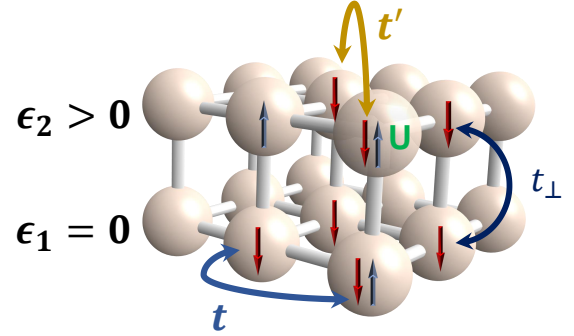


FIG. 1. Schematic diagram of the imbalanced bilayer Hubbard model. The blue and yellow arrows represent nearest-neighbor and next-nearest-neighbor hoppings respectively and the dark arrow indicates the interlayer hybridization. The onsite energy  $\epsilon_2 > 0$  is introduced to tune the density imbalance between layers.

This concept has generated considerable interest in understanding how multilayer systems can enhance the superconducting critical temperature  $T_c$ . For instance, enhanced SC has been observed in superlattice systems with repulsive Coulomb interaction [37, 38], as well as in composite superconductor/metal bilayers with attractive Coulomb interactions [39, 40], where  $T_c$  exceeds that of single-layer systems [37]. Similarly, prior work on composite superconductors suggested that minimizing the thickness of the metallic layer can suppress phase fluctuations, thereby maximizing  $T_c$  [41].

Motivated by these findings, we investigate the bilayer Hubbard model with repulsive onsite interactions to explore how imbalanced electron densities across the two layers influence the SC properties. Specifically, we not only map out the transition between  $d$ -wave and  $s^\pm$ -wave pairing symmetries at weak-to-intermediate hybridization strengths but also identify higher  $T_c$  in systems with imbalanced electron densities. We systematically analyze the relationship between  $T_c$  and

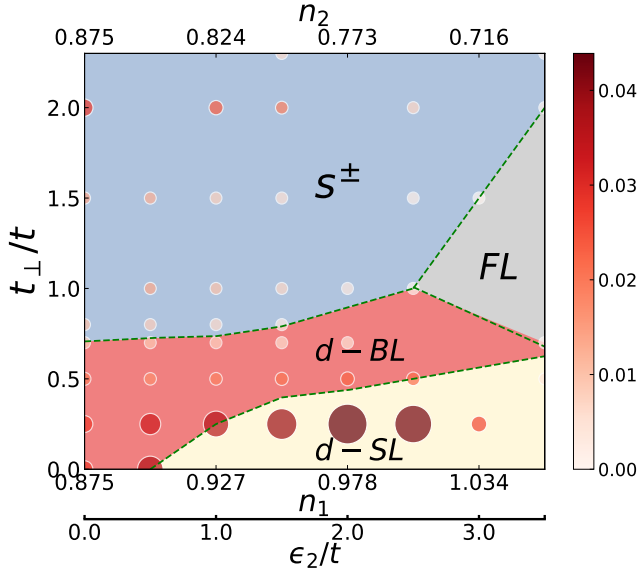


FIG. 2. The density versus interlayer hybridization phase diagram of imbalanced bilayer Hubbard model consists of  $d$ -wave on both layers ( $d$ -BL),  $d$ -wave on single layer ( $d$ -SL) with lower doping, and  $s^\pm$ -wave SC phases. The estimated phase boundaries are denoted by dashed green lines. The magnitude of  $T_c$  is indicated by the size and color of circles. The fixed average electron density is  $n = 0.875$ .

electron density distribution, as well as the SC phase transition driven by interlayer hybridization. This paper is organized as follows: Section II introduces the model and methodology; Section III presents the phase diagram and associated properties of  $s^\pm$ -wave and  $d$ -wave pairings; and Section IV provides the summary and outlook.

## II. MODEL AND METHOD

### A. Imbalanced Bilayer Hubbard model

We consider the bilayer Hubbard model on a two-dimensional square lattice as shown in Fig. 1 with the Hamiltonian

$$\begin{aligned}
 H = & -t \sum_{\langle ij \rangle \sigma m} c_{im\sigma}^\dagger c_{jm\sigma} - t' \sum_{\langle\langle ij \rangle\rangle \sigma m} c_{im\sigma}^\dagger c_{jm\sigma} \\
 & - t_\perp \sum_{i\sigma} c_{i1\sigma}^\dagger c_{i2\sigma} + \text{H.c.} \\
 & + U \sum_{im} n_{im\uparrow} n_{im\downarrow} + \sum_{i\sigma m} (\epsilon_2 \delta_{m2} - \mu) n_{im\sigma}
 \end{aligned}$$

where  $c_{i\sigma}^\dagger$  ( $c_{i\sigma}$ ) creates (annihilates) an electron with spin  $\sigma$  ( $=\uparrow, \downarrow$ ) in  $m$ -th ( $=1, 2$ ) layer at site  $i$ . We set the intralayer nearest-neighbor hopping  $t = 1$  as the unit of energy. The conventional parameters for the

intralayer next-nearest-neighbor hopping  $t' = -0.15t$  and on-site Coulomb interaction  $U = 7t$  are adopted [30, 42]. The chemical potential  $\mu$  fixes the average density, which is chosen at a characteristic  $n = 0.875$  throughout the present work for simplicity. Other average densities without might not induce significant difference from our presented results below. Two important parameters include the additional site energy ( $\epsilon_2$ ) to adjust the electron density imbalance as well as the tunable interlayer hybridization  $t_\perp$ . Notably, the density distribution remains nearly unaffected by the hybridization (see Appendix Fig. 11).

### B. Dynamical cluster approximation (DCA)

DCA with the continuous-time auxiliary-field (CT-AUX) quantum Monte Carlo (QMC) cluster solver [43–46] is employed to numerically solve the bilayer model. As a celebrated quantum many-body numerical method, the DCA evaluates various physical observables in the thermodynamic limit by mapping the bulk lattice problem onto a finite cluster embedded in a mean-field bath in a self-consistent manner [43, 44], which is realized by the convergence between the cluster and coarse-grained (averaged over a patch of the Brillouin zone around a specific cluster momentum  $\mathbf{K}$ ) single-particle Green's functions. In particular, the short-range interactions within the cluster are treated exactly with various numerical techniques, e.g. CT-AUX used in the present study; while the longer-ranged physics is approximated by a mean field hybridized with the cluster. Therefore, increasing the cluster size systematically approaches the exact result in the thermodynamic limit. The finite cluster size essentially approximates the whole Brillouin zone by a discrete set of  $\mathbf{K}$  points so that the self-energy  $\Sigma(\mathbf{K}, i\omega_n)$  is a constant function within the patch around a particular  $\mathbf{K}$  and a step function in the whole Brillouin zone. Generically, the quantum embedding methods including DCA have a better minus sign problem than the finite-size QMC simulations because of the hosting mean field. Most of our calculations were conducted with  $N_c = 16 (= 8 \times 2)$ -site DCA cluster to incorporate the momentum space resolution including in-plane nodal  $\mathbf{K} = (\pi/2, \pi/2)$  and antinodal  $\mathbf{K} = (\pi, 0)$  directions.

### C. Bethe-Salpeter equation (BSE)

The superconducting properties can be studied by solving the Bethe-Salpeter equation (BSE) in its eigen-equation form in the particle-particle channel [47, 48]

$$-\frac{T}{N_c} \sum_{K'} \Gamma^{pp}(K, K') \bar{\chi}_0^{pp}(K') \phi_\alpha(K') = \lambda_\alpha(T) \phi_\alpha(K) \quad (1)$$

where  $\Gamma^{pp}(K, K')$  denotes the irreducible particle-particle vertex of the effective cluster problem, with

$K = (\mathbf{K}, i\omega_n)$  combining the cluster momenta  $\mathbf{K}$  and Matsubara frequencies  $\omega_n = (2n + 1)\pi T$ , and  $\phi_\alpha(K)$  represents the eigenvector solved from BSE with the  $\alpha$ -wave pairing symmetry.

The coarse-grained bare particle-particle susceptibility

$$\bar{\chi}_0^{pp}(K) = \frac{N_c}{N} \sum_{k'} G(K + k') G(-K - k') \quad (2)$$

is obtained via the dressed single-particle Green's function,

$$G(k) \equiv G(\mathbf{k}, i\omega_n) = [i\omega_n + \mu - \varepsilon_{\mathbf{k}} - \Sigma(\mathbf{K}, i\omega_n)]^{-1} \quad (3)$$

where  $\mathbf{k}$  belongs to the DCA patch surrounding the cluster momentum  $\mathbf{K}$  with the chemical potential  $\mu$ ,  $\varepsilon_{\mathbf{k}} = -2t(\cos k_x + \cos k_y) - 4t' \cos k_x \cos k_y$  the dispersion relation, and  $\Sigma(\mathbf{K}, i\omega_n)$  the cluster self-energy. In practice, we calculate 32 or more discrete points for both the positive and negative fermionic Matsubara frequency  $\omega_n = (2n + 1)\pi T$  mesh for measuring the two-particle Green's functions and irreducible vertices. Therefore, the BSE Eq. (1) reduces to an eigenvalue problem of a matrix of size  $(64N_c) \times (64N_c)$ .

To systematically investigate the interplay between interlayer hybridization and density imbalance, we first analyze the temperature evolution of the BSE eigenvalue  $\lambda_\alpha(T)$  ( $\alpha = d, s^\pm$ ). The observation of BCS-like logarithmic temperature dependence would indicate behavior analogous to that observed in the  $d$ -wave superconducting phase of the conventional single-band Hubbard model in the overdoped regime [42]. Conversely, the emergence of linear or exponential temperature dependence would suggest non-BCS pairing fluctuations, similar to those characteristic of the pseudogap regime in the single-band model [42].

### III. RESULTS

Our main result is shown in the phase diagram Fig. 2, which consists of the  $d$ -wave and  $s^\pm$ -wave SC phases controlled by the hybridization  $t_\perp$  and electron density imbalance tuned by  $\epsilon_2$ . At large  $t_\perp$ , the bilayer system is dominated by the interlayer pairing so that  $s^\pm$ -wave until large enough density imbalance finally destroys the SC to results in a Fermi liquid. Interestingly, at small  $t_\perp$ , apart from the conventional regimes of  $d$ -wave pairing on both layers ( $d$ -BL), there exists a sizable regime with  $d$ -wave pairing solely on single layer ( $d$ -SL). More intriguingly, the globally optimal  $T_c$  is within this  $d$ -SL phase, which is reminiscent of our recent work of the trilayer Hubbard model [49]. While the estimated phase boundaries denoted by dashed green lines are solely based on our finite number of simulated parameters points, it is reasonable to expect its physical plausibility. For clarity, the magnitude of  $T_c$  is indicated by both the size and color of the circles.

In the following subsections, we provide a detailed analysis of both  $s^\pm$ -wave and  $d$ -wave superconducting pairing under varying hybridization strengths and density imbalance conditions. Unless explicitly noted otherwise, all calculations are performed at a fixed average electron density of  $n = 0.875$ .

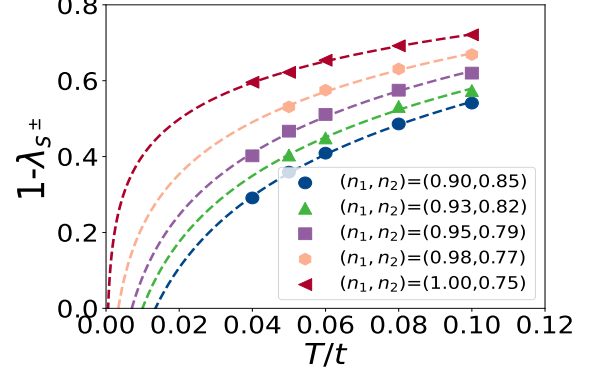


FIG. 3. Temperature evolution of  $1 - \lambda_{s^\pm}(T)$  for varying density distribution at the characteristic  $t_\perp/t = 1.0$ .

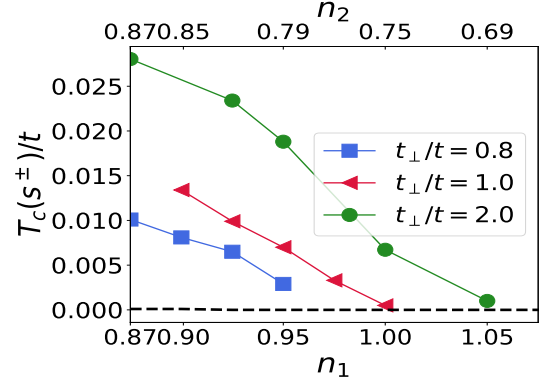


FIG. 4. The density evolution of  $s^\pm$ -wave pairing  $T_c$  at the three characteristic hybridization  $t_\perp/t = 0.8, 1.0$  and  $2.0$ .

#### A. $s^\pm$ -wave pairing at large hybridization

We first focus on the large  $t_\perp$  regime where the  $s^\pm$ -wave pairing dominates. In Fig. 3, we present the extrapolated  $1 - \lambda_{s^\pm}(T)$  curves for various density distributions at the characteristic hybridization  $t_\perp/t = 1.0$ . All curves show the logarithmic dependence even though one layer's density readily resides in the underdoped regime in the context of single-layer model. Besides, the pairing instability apparently weakens with the density imbalance monotonically.

The  $T_c(s^\pm)$  is expected to decrease as the density imbalance increases. To elucidate this trend, Fig. 4 explicitly reveals that  $T_c$  decays linearly with the density

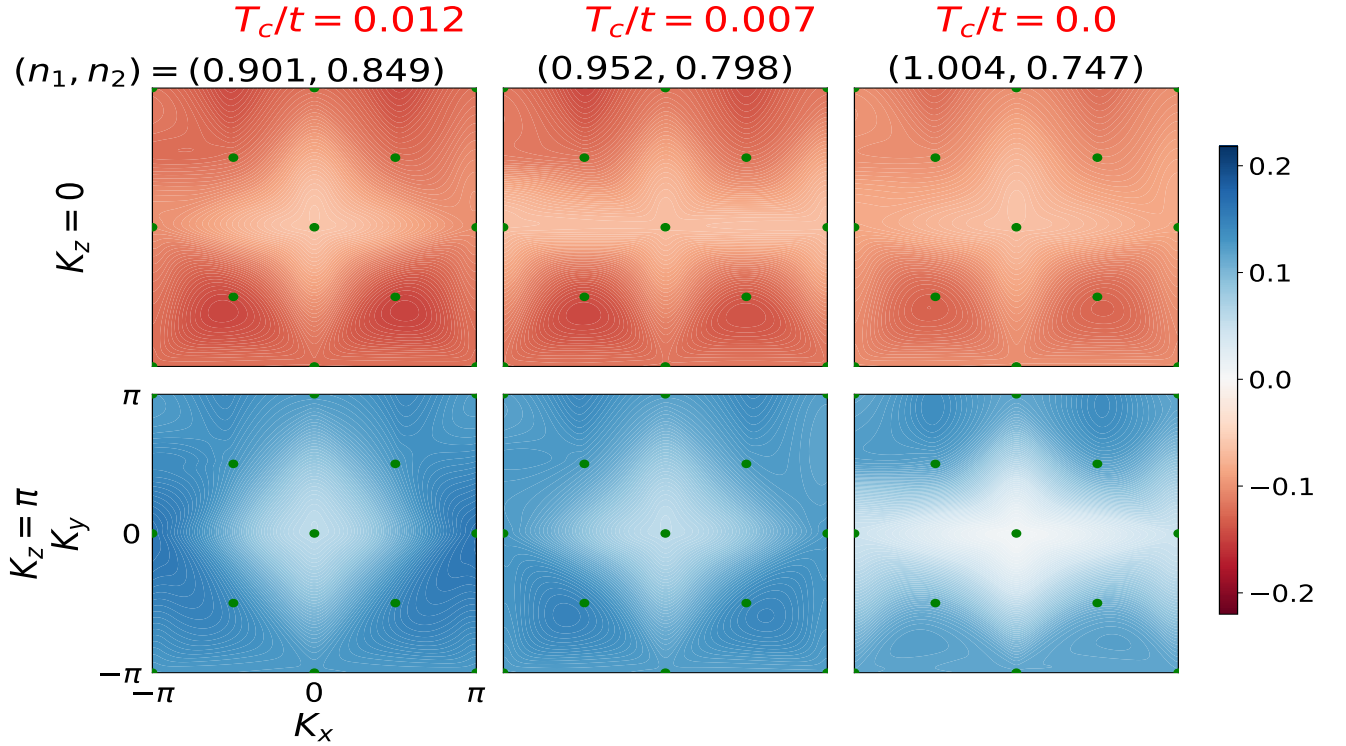


FIG. 5. The eigenvector  $\phi_{s\pm}(\mathbf{K}, \pi T)$  of bonding ( $\mathbf{K}_z = 0$ ) and anti-bonding ( $\mathbf{K}_z = \pi$ ) at the lowest simulated temperature  $T/t = 0.04$  for various density distributions at  $t_{\perp}/t = 1.0$ .

so that also the imbalance at large  $t_{\perp}$ . Given that the  $s^{\pm}$ -wave pairing originates from the interlayer hybridization, the large density imbalance naturally suppresses the pairing, as further confirmed by the weakening of the BSE eigenvector (as a normal state analog of SC gap function) of both the bonding ( $\mathbf{K}_z = 0$ ) and anti-bonding ( $\mathbf{K}_z = \pi$ ) bands shown in Fig. 5. We remark that the eigenvectors are at a fixed temperature above  $T_c$  so that  $\phi_{s\pm}$  still shows the characteristic feature for  $s^{\pm}$  pairing even though the estimated  $T_c$  is zero, which can be hinted as the gradual vanishing of  $\phi_{s\pm}$  in the anti-bonding band. Note also that  $T_c(s^{\pm})$  is generically lower than its  $d$ -wave counterpart.

### B. $d$ -wave pairing with enhanced $T_c$

We next switch to the small  $t_{\perp}$  regime where the  $d$ -wave pairing will dominate over the  $s^{\pm}$ -wave. The logarithmic  $1 - \lambda_d(T)$  curves in Fig. 6 reveal the density distribution and hybridization dependence distinct from Fig. 3. Specifically, the density imbalance between the two layers enhances the  $d$ -wave pairing instability, but this instability weakens with increasing hybridization strength. In particular, the pairing reaches its maximum when the UL reaches around half-filling, followed by a sharp decrease upon exceeding this filling level, for example, at  $t_{\perp} = 0.5$ . One possibility for this “critical

half-filling” might be the nature from hole to electron doping beyond this point.

As shown in Fig. 7, the  $T_c$  for  $d$ -wave pairing decreases monotonically with increasing hybridization from  $t_{\perp}/t = 0.25$  to 0.7 in all density distributions examined, in contrast to the trend observed for  $s^{\pm}$ -wave pairing as discussed above. Most notably, the  $T_c$  curves in Fig. 7 exhibit a non-monotonic dependence on density imbalance before vanishing at sufficiently large  $n_1 - n_2$ , with this critical value decreasing monotonically with  $t_{\perp}$ . Note that although the optimal  $T_c$ , surpassing the density-balanced value, occurs when the UL density approaches half-filling  $n_1 \sim 1.0$  at  $t_{\perp}/t = 0.25, 0.5$ , which coincides with Fig. 6, this feature disappears at  $t_{\perp}/t = 0.7$ . Hence, we believe that the optimal  $n_1$  cannot exceed half-filling to be within the electron-doping side. In addition, the magnitude of the  $T_c$ ’s rise weakens with enlarged  $t_{\perp}$ . However, it is unclear why there is a slightly drop with the  $(n_1, n_2) = (0.9, 0.85)$  at  $t_{\perp}/t = 0.5$ .

Concurrently, as shown in Fig. 8, the  $d$ -wave eigenvector  $\phi_d$  in the OL disappears when its density decreases, while the the UL demonstrates a non-monotonic evolution, initially strengthening and subsequently weakening. Therefore, we contend that the mechanism of  $T_c$  enhancement in the imbalance bilayer model could be potentially accounted for by the composite picture [35], where the UL hosts the large pairing scale and the OL provides the strong phase stiffness. The highest  $T_c$  likely originates from the



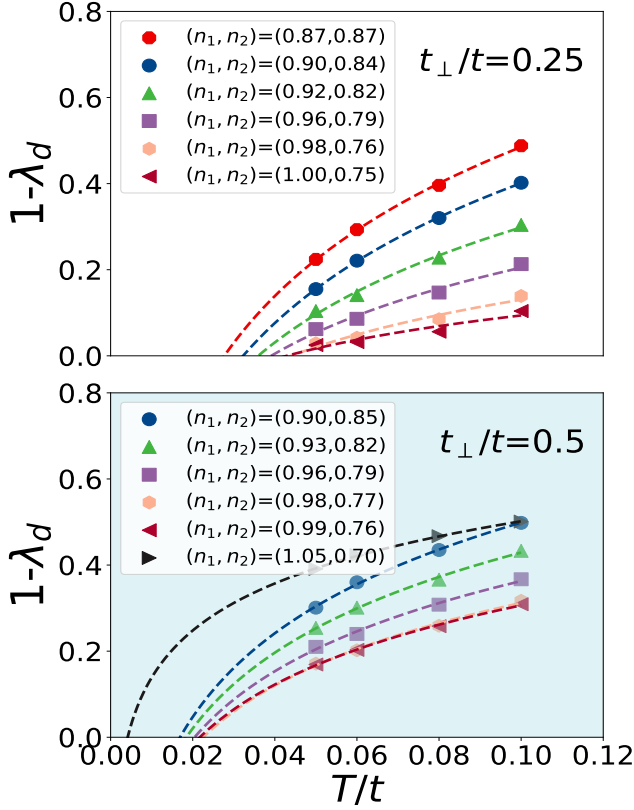


FIG. 6. Temperature evolution of  $1 - \lambda_d(T)$  for varying density distribution at two characteristic hybridization  $t_{\perp}/t = 0.25$  and  $0.5$ .

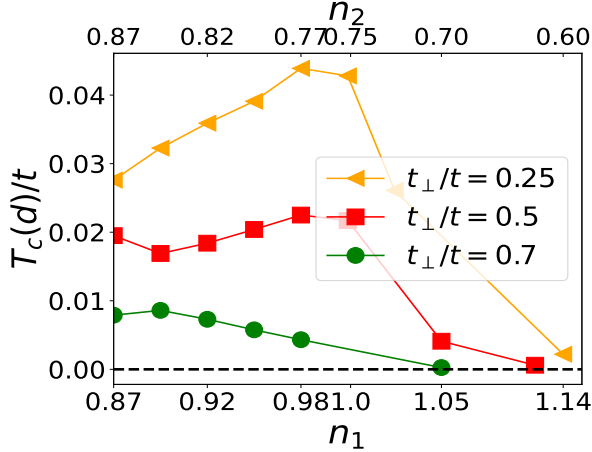


FIG. 7. Density distribution dependency of  $d$ -wave pairing SC critical temperature  $T_c$  at three fixed hybridization  $t_{\perp}/t = 0.25, 0.5$  and  $0.7$ .

maximal pairing in the nearly half-filled UL combined with the phase stiffness contributions from the OL.

Moreover, to better characterize the deviation between two layers and fully examine the density imbalance dependence of the  $d$ -SL phase, we introduce the  $D$  value [49], defined as the  $d$ -wave projection of the BSE

eigenvector  $\phi_d$  [49, 50]

$$D = \sum_{\mathbf{K}} g(\mathbf{K}) \phi_d(\mathbf{K}, \pi T)$$

with  $g(\mathbf{K}) = \cos \mathbf{K}_x - \cos \mathbf{K}_y$ . This observable can be used to quantify the difference in  $d$ -wave pairing strength across the UL and OL.

Fig. 9 shows that with decreasing OL's density, the corresponding  $D$  decays asymptotically to zero, whereas the UL's  $D$  grows monotonically with increasing density until the saturation, resulting in a splitting behavior due to their density imbalance. This splitting is partially suppressed by interlayer hybridization. Interestingly, at  $t_{\perp}/t = 0.25$ , beyond a critical density  $(n_1, n_2) = (0.927, 0.824)$ , the OL exhibits a vanishing  $D$ , indicating complete suppression of its  $d$ -wave pairing. Meanwhile, the  $D$  of the UL starts to saturate. Intriguingly, despite of this loss of normal state “gap” (BSE eigenvector) in the OL, Fig. 7 reveals that the  $T_c$  continues to rise, reaching its maximum whose  $d$ -wave SC is solely hosted in the UL. This observation suggests that the  $d$ -wave pairing SC is divided into two distinct phases, labeled as  $d-SL$  and  $d-BL$  in Fig. 2, with the highest  $T_c$  achieved in the former. According to Fig. 12 in Appendix, it is observed that with increasing density difference  $(n_1 - n_2)$ , the  $d$ -wave SC phase diminishes and eventually transitions into the Fermi liquid phase as shown in Fig. 2.

### C. SC pairing symmetry transition

The previous work [28] has demonstrated a superconducting pairing symmetry transition from  $d$ -wave to  $s^{\pm}$ -wave. Similarly, in our imbalanced bilayer model, we observe both  $s^{\pm}$ -wave pairing at large hybridization (Fig. 5) and  $d$ -wave pairing at weak hybridization (Fig. 8), indicating the existence of such SC pairing transitions.

Fig. 10 illustrates the non-monotonic dependence of the extracted  $T_c$  on the hybridization strength at a fixed density distribution  $(n_1, n_2) = (0.952, 0.798)$ . The curve reveals markedly different sensitivities of  $d$ -wave and  $s^{\pm}$ -wave pairing to the hybridization. The analysis of layer-resolved pairing reveals that at small  $t_{\perp}$  values ( $d$ -SL regime in Fig. 2),  $d$ -wave pairing occurs exclusively in the UL, yielding the optimal  $T_c$ .

In contrast, the larger interlayer hybridization induces  $d$ -wave pairing in both layers ( $d-BL$  region), albeit with reduced pairing strength in each individual layer as shown in Fig. 9. While  $s^{\pm}$ -wave pairing gradually enhances at intermediate hybridization ( $t_{\perp}/t = 0.8$ ) and reached its optimal pairing conditions at  $t_{\perp}/t = 2.0$ , this instability is gradually destroyed by stronger hybridization, consistent with our previous work on the balanced bilayer model [30]. As shown in Fig. 2, the critical hybridization strength increases with the density difference  $(n_1 - n_2)$ . Importantly, the highest  $T_c$  achieved

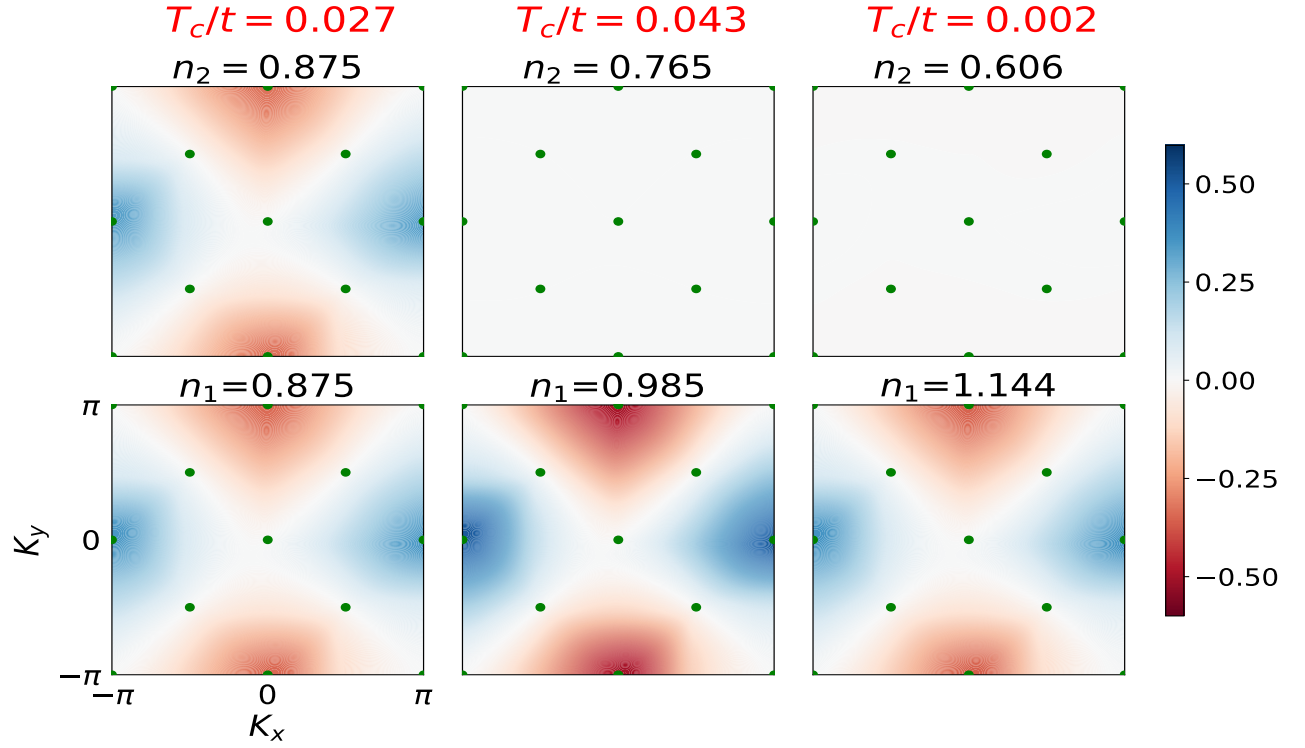


FIG. 8. The eigenvector  $\phi_d(\mathbf{K}, T)$  of the OL (upper) and the UL (lower) at the lowest simulated temperature  $T/t = 0.05$  for various density distributions at  $t_{\perp}/t = 0.25$ .

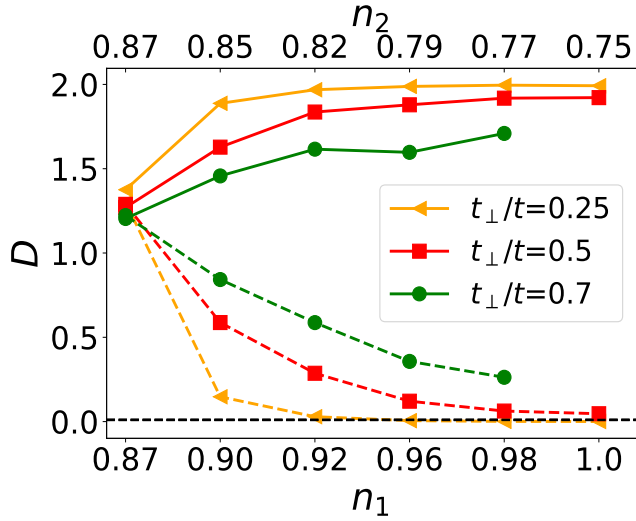


FIG. 9. The electron density evolution of  $D$  value for the UL (solid line) and the OL (dashed line) at three fixed hybridization  $t_{\perp}/t = 0.25, 0.5, 0.7$  under the lowest simulated temperature  $T/t = 0.05$ .

for  $d$ -wave pairing generally exceeds that of  $s^{\pm}$ -wave pairing.

At sufficiently high density imbalance, the system transits into a Fermi liquid state, as indicated by the

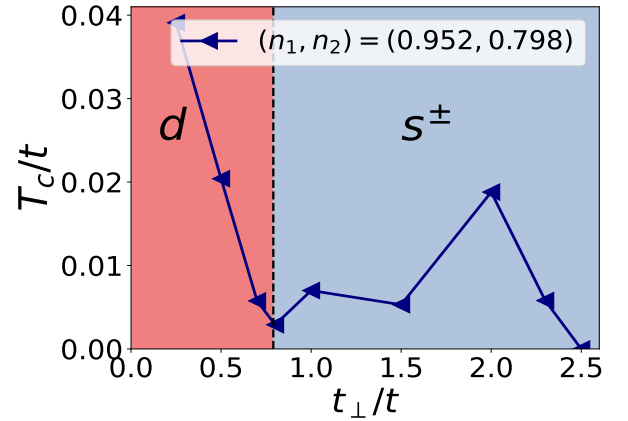


FIG. 10. The hybridization dependence of  $T_c$  at a characteristic density distribution  $(n_1, n_2 = 0.952, 0.798)$ . The  $d$ -wave pairing and  $s^{\pm}$ -wave pairing are divided by the dashed line at  $t_{\perp}/t = 0.8$ .

temperature-dependent zero-frequency Green function and frequency-dependent self-energy, which will be discussed more in Fig. 13 of Appendix.

#### IV. SUMMARY AND OUTLOOK

In summary, we performed the dynamical cluster quantum Monte Carlo simulations to systematically explore the effects of the interlayer hybridization and density imbalance on superconducting properties in imbalanced bilayer system.

The mapped rich phase diagram in Fig. 2 reveals the competition between  $d$ -wave and  $s^\pm$ -wave SC. Intriguingly, it is discovered that the density imbalance is beneficial to the  $d$ -wave SC and can potentially boost  $T_c$  for a wide range of density imbalance. Moreover, the enhanced SC can be solely hosted by one layer with lower hole doping, which is reminiscent of our recent investigation of the trilayer Hubbard model [49]. This suggests that the  $T_c$  enhancement can be accomplished via generic density imbalance in a composite layered system so that the composite picture [35] provides the plausible framework for interpreting the enhanced  $T_c$ . In this picture, the other layer without SC gap opening is essential for the  $T_c$  enhancement although our present temperature scale cannot reach decisive conclusions regarding its mechanism responsible for it. It is, however, reasonable to expect that the BSE eigenvector of the OL can open the  $d$ -wave gap in lower temperatures. Put another way, our observation that the BSE eigenvector does not exhibit significant weight on the OL is not a proof that the superfluid stiffness is not established by tunneling into this layer. Other advanced many-body methods are strongly desired for resolving these issues.

For the  $s^\pm$ -wave pairing regime at large hybridization  $t_\perp$ , the highest  $T_c$  emerges at balanced system and the density imbalance is generally detrimental to SC because of the interlayer pairing nature of  $s^\pm$ -wave SC. One interesting extension is to explore if the previously conjectured coexistence of  $d$ -wave and  $s^\pm$ -wave pairing [28] can be stabilized in the presence of density balance.

Given that the bilayer model is relevant to various context of physical systems such as real materials and ultracold atomic systems[4, 32–34, 51], it is anticipated that the present study on the influence of the density imbalance provides more insight on this well-established model, especially in terms of the  $T_c$  enhancement and its connection to the composite picture.

#### V. ACKNOWLEDGEMENT

We would like to thank Xianxin Wu, Jun Zhan, and Fan Yang for illuminating discussions. We acknowledge the support by National Natural Science Foundation of China (NSFC) Grant No. 12174278.

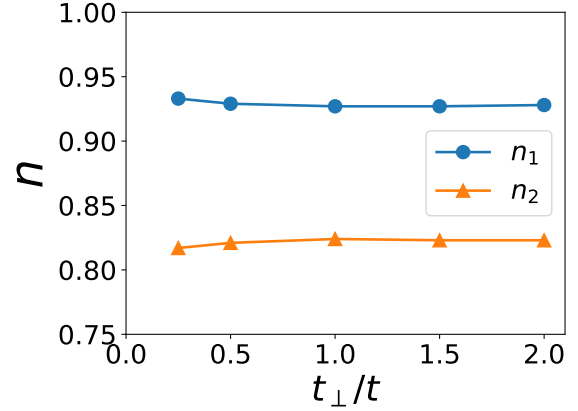


FIG. 11. The hybridization dependence of the density distribution at  $\epsilon_2 = 1.0t$ .

#### VI. APPENDIX

##### A. Hybridization independent density distribution

Fig. 11 displays the calculated density distribution for a representative set of parameters ( $\epsilon_2 = 1.0t$  and  $t_\perp/t$  varies from 0.25 to 2.0). The density of each layer almost keeps unchanged so that when we use the parameter  $\epsilon_2$  to adjust the density distribution in the bilayer model, the influence of  $t_\perp$  on the density distribution is negligible. This provides a convenient way to study the effect of density distribution on SC for different hybridizations.

##### B. Single-particle Green function and self-energy

To investigate the metallic or insulating nature upon suppressing the SC phase via interplay between the density distribution and hybridization, we examine the spectral function  $A(k, \omega = 0) = -\frac{1}{\pi} \text{Im}G(k, \omega = 0)$  by linearly extrapolating to the zero imaginary-frequency limit from the two lowest Matsubara frequencies of  $\text{Im}G(\mathbf{K}, i\omega_n)$  (accurately computed using the DCA method) [30, 52, 53]. This extrapolated value serves as a reliable proxy for the spectral function  $A(k, \omega = 0)$  at zero real frequency.

The convergence of  $\text{Im}\Sigma(\mathbf{K}, i\omega_n)$  to a finite value as  $i\omega_n \rightarrow 0$  is a typical non-Fermi liquid behavior; while the diverging or decaying behavior indicate the gap opening originating from strong correlation or gap closing separately [54] at the particular  $\mathbf{K}$  point. Here, we focus on the nodal  $\mathbf{K} = (\frac{\pi}{2}, \frac{\pi}{2})$  and antinodal  $\mathbf{K} = (\pi, 0)$  points included in our adopted DCA cluster.

As illustrated by the extrapolated single-particle Green function in Fig. 12, the OL consistently exhibits Fermi liquid behavior across all density distributions at  $t_\perp/t = 0.25$ . In contrast, the UL initially displays Fermi liquid behavior since both nodal and antinodal directions

manifest the increasing values with lowering  $T$ . The UL then develops an energy gap at larger density imbalance, e.g.  $(n_1, n_2) = (0.96, 0.79)$ , before eventually returning to Fermi liquid behavior as one layer realizes the electron doping. The divergent imaginary part of self-energy observed for the UL at  $(n_1, n_2) = (0.999, 0.751)$  further corroborates the emergence of strong correlation induced pseudogap opening. The self-energy of OL indicates the strongly renormalized electronic interaction so that metallic character.

Regarding the ultimate electronic state of the  $s^\pm$ -wave superconducting phase under sufficiently large density disparities (as established in the main text), Fig. 13 demonstrates two key features: (i) the bonding band persistently retains its Fermi liquid character irrespective of density distribution, whereas (ii) the anti-bonding band manifests obvious momentum-dependent behavior. Crucially, the self-energy reveals weakly correlated electron interactions in both bands. These observations collectively suggest a quantum phase transition from the  $s^\pm$ -wave pairing SC to a Fermi liquid phase beyond the critical density imbalance in Fig. 2.



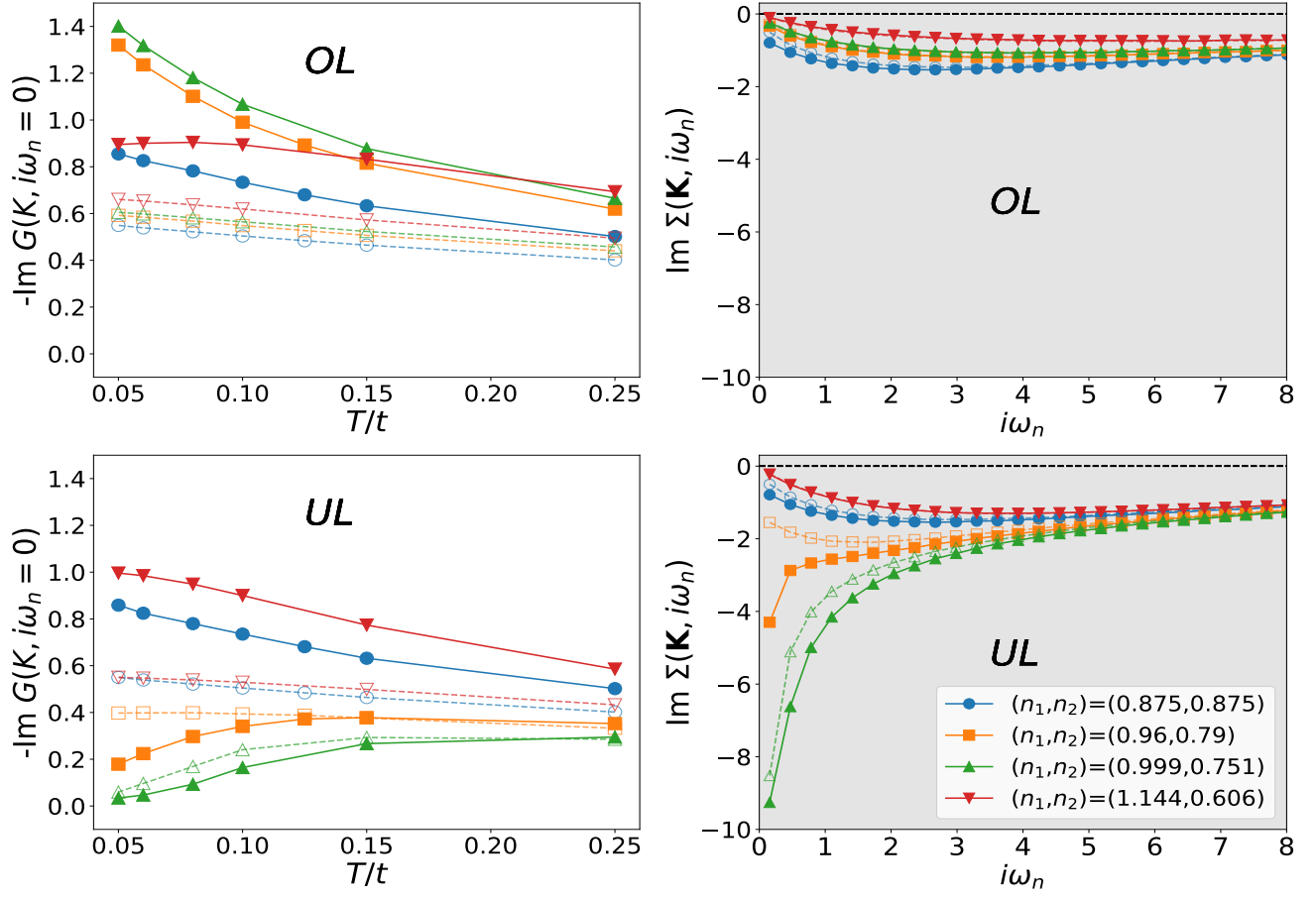


FIG. 12. Temperature evolution of the extrapolated imaginary zero-frequency  $-\text{Im}G(\mathbf{K}, i\omega_n = 0)$  obtained from a linear extrapolation of the first two Matsubara frequencies (white panels) and the imaginary part of self-energy  $\text{Im}\Sigma(\mathbf{K}, i\omega_n)$  at  $T/t = 0.05$  (gray panels) for the OL (upper panels) and UL (lower panels). The dashed and solid lines represent nodal ( $\pi/2, \pi/2$ ) and antinodal ( $\pi, 0$ ) directions for various density distributions. The hybridization is  $t_\perp/t = 0.25$  within the  $d$ -wave pairing regime.

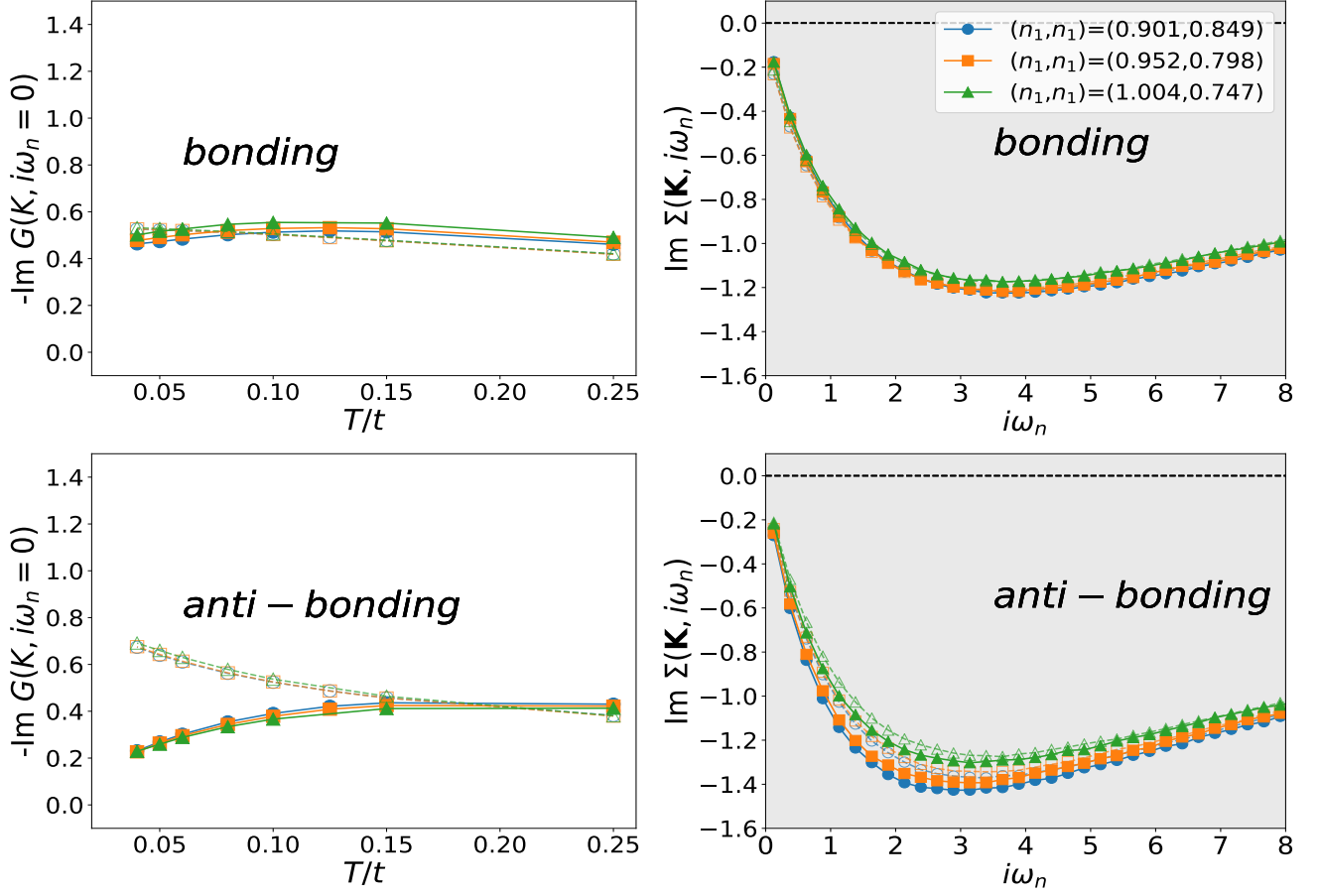


FIG. 13. Temperature evolution of the extrapolated imaginary zero-frequency  $-\text{Im} G(\mathbf{K}, i\omega_n = 0)$  obtained from a linear extrapolation of the first two Matsubara frequencies (white panels) and the imaginary part of self-energy  $\text{Im} \Sigma(\mathbf{K}, i\omega_n)$  at  $T/t = 0.04$  (gray panels) for the bonding (upper panels) and anti-bonding band (lower panels). The dashed and solid lines represent nodal  $(\pi/2, \pi/2)$  and antinodal  $(\pi, 0)$  directions for various density distributions. The hybridization is  $t_\perp/t = 1.0$  within the  $s^\pm$ -wave pairing regime.

- 
- [1] N. Bulut, D. J. Scalapino, and R. T. Scalettar, Nodeless d-wave pairing in a two-layer Hubbard model, *Phys. Rev. B* **45**, 5577 (1992).
- [2] R. T. Scalettar, J. W. Cannon, D. J. Scalapino, and R. L. Sugar, Magnetic and pairing correlations in coupled Hubbard planes, *Phys. Rev. B* **50**, 13419 (1994).
- [3] R. R. dos Santos, Magnetism and pairing in Hubbard bilayers, *Phys. Rev. B* **51**, 15540 (1995).
- [4] M. Gall, N. Wurz, J. Samland, C. F. Chan, and M. Köhl, Competing magnetic orders in a bilayer Hubbard model with ultracold atoms, *Nature* **589**, 40 (2021).
- [5] S. Karakuzu, S. Johnston, and T. A. Maier, Superconductivity in the bilayer Hubbard model: Two Fermi surfaces are better than one, *Phys. Rev. B* **104**, 245109 (2021).
- [6] T. I. Vanhala, J. E. Baarsma, M. O. J. Heikkinen, M. Troyer, A. Harju, and P. Törmä, Superfluidity and density order in a bilayer extended Hubbard model, *Phys. Rev. B* **91**, 144510 (2015).
- [7] M. Golor and S. Wessel, Nonlocal density interactions in auxiliary-field quantum Monte Carlo simulations: Application to the square lattice bilayer and honeycomb lattice, *Phys. Rev. B* **92**, 195154 (2015).
- [8] G. Hildebrand, E. Arrigoni, W. Hanke, and J. Schmalian, Magnetic fluctuations in coupled inequivalent Hubbard layers as a model for  $\text{Y}_2\text{Ba}_4\text{Cu}_7\text{O}_{15}$ , *European Physical Journal. B* **8**, 195–205 (1999).
- [9] A. Euverte, S. Chiesa, R. T. Scalettar, and G. G. Batrouni, Magnetic transition in a correlated band insulator, *Phys. Rev. B* **87**, 269 (2013).
- [10] R. Rüger, L. F. Tocchio, R. Valentí, and C. Gros, The phase diagram of the square lattice bilayer Hubbard model: a variational Monte Carlo study, *New Journal of Physics* **16**, 033010 (2014).
- [11] H. Sun, M. Huo, X. Hu, J. Li, Z. Liu, Y. Han, L. Tang, Z. Mao, P. Yang, B. Wang, *et al.*, Signatures of superconductivity near 80 K in a nickelate under high pressure, *Nature* **621**, 493 (2023).
- [12] L. F. Lin, Y. Zhang, N. Kaushal, G. Alvarez, T. A. Maier, A. Moreo, and E. Dagotto, Magnetic phase diagram of a two-orbital model for bilayer nickelates with varying doping, *Phys. Rev. B* **110**, 195135 (2024).
- [13] Y.-Y. Zheng and W. Wú,  $s^\pm$ -wave superconductivity in the bilayer two-orbital Hubbard model, *Phys. Rev. B* **111**, 035108 (2025).
- [14] W. Xi, S.-L. Yu, and J.-X. Li, Transition from  $s_\pm$ -wave to  $d_{x^2-y^2}$ -wave superconductivity driven by interlayer interaction in the bilayer two-orbital model of  $\text{La}_3\text{Ni}_2\text{O}_7$ , *Phys. Rev. B* **111**, 104505 (2025).
- [15] T. A. Maier, P. Doak, L.-F. Lin, Y. Zhang, A. Moreo, and E. Dagotto, Interlayer Pairing in Bilayer Nickelates (2025), [arXiv:2506.07741](https://arxiv.org/abs/2506.07741).
- [16] J. Yang, H. Sun, X. Hu, Y. Xie, T. Miao, H. Luo, H. Chen, B. Liang, W. Zhu, G. Qu, C.-Q. Chen, M. Huo, Y. Huang, S. Zhang, F. Zhang, F. Yang, Z. Wang, Q. Peng, H. Mao, G. Liu, Z. Xu, T. Qian, D.-X. Yao, M. Wang, L. Zhao, and X. J. Zhou, Orbital-dependent electron correlation in double-layer nickelate  $\text{La}_3\text{Ni}_2\text{O}_7$ , *Nature Communications* **15**, 4373 (2024).
- [17] M. Wang, H.-H. Wen, T. Wu, D.-X. Yao, and T. Xiang, Normal and Superconducting Properties of  $\text{La}_3\text{Ni}_2\text{O}_7$ , *Chin. Phys. Lett.* **41**, 077402 (2024).
- [18] C. Lu, Z. Pan, F. Yang, and C. Wu, Interlayer-coupling-driven high-temperature superconductivity in  $\text{La}_3\text{Ni}_2\text{O}_7$  under pressure, *Phys. Rev. Lett.* **132**, 146002 (2024).
- [19] Z. Luo, B. Lv, M. Wang, W. Wú, and D.-X. Yao, High-TC superconductivity in  $\text{La}_3\text{Ni}_2\text{O}_7$  based on the bilayer two-orbital t-J model, *npj Quantum Materials* **9**, 61 (2024).
- [20] S. Bötzel, F. Lechermann, J. Gondolf, and I. M. Eremin, Theory of magnetic excitations in the multilayer nickelate superconductor  $\text{La}_3\text{Ni}_2\text{O}_7$ , *Phys. Rev. B* **109**, L180502 (2024).
- [21] Y. Zhang, L.-F. Lin, A. Moreo, T. A. Maier, and E. Dagotto, Trends in electronic structures and  $s_\pm$ -wave pairing for the rare-earth series in bilayer nickelate superconductor  $\text{R}_3\text{Ni}_2\text{O}_7$ , *Phys. Rev. B* **108**, 165141 (2023).
- [22] Q.-G. Yang, D. Wang, and Q.-H. Wang, Possible  $s_\pm$ -wave superconductivity in  $\text{La}_3\text{Ni}_2\text{O}_7$ , *Phys. Rev. B* **108**, L140505 (2023).
- [23] Z. Liao, L. Chen, G. Duan, Y. Wang, C. Liu, R. Yu, and Q. Si, Electron correlations and superconductivity in  $\text{La}_3\text{Ni}_2\text{O}_7$  under pressure tuning, *Phys. Rev. B* **108**, 214522 (2023).
- [24] X. Chen, J. Zhang, A. S. Thind, S. Sharma, H. LaBollita, G. Peterson, H. Zheng, D. P. Phelan, A. S. Botana, R. F. Klie, and J. F. Mitchell, Polymorphism in the ruddlesden–popper nickelate  $\text{La}_3\text{Ni}_2\text{O}_7$ : Discovery of a hidden phase with distinctive layer stacking, *J. Am. Chem. Soc.* **146**, 3640 (2024).
- [25] L. Rademaker, S. Johnston, J. Zaanen, and V. D. B. Jeroen, Determinant quantum monte carlo study of exciton condensation in the bilayer Hubbard model, *Phys. Rev. B* **88**, 235115 (2013).
- [26] J. P. Eisenstein and A. H. Macdonald, Bose–einstein condensation of excitons in bilayer electron systems, *Nature* **432**, 691 (2004).
- [27] X. X. Huang, M. Claassen, E. W. Huang, B. Moritz, and T. P. Devereaux, Biexciton condensation in electron-hole-doped Hubbard bilayers: A sign-problem-free quantum monte carlo study, *Phys. Rev. Lett.* **124**, 077601 (2020).
- [28] T. A. Maier and D. J. Scalapino, Pair structure and the pairing interaction in a bilayer Hubbard model for unconventional superconductivity, *Phys. Rev. B* **84**, 180513 (2011).
- [29] V. Mishra, D. J. Scalapino, and T. A. Maier,  $s^\pm$  pairing near a Lifshitz transition, *Scientific Reports* **6** (2016).
- [30] X. Liu and M. Jiang, Hybridization-induced quantum phase transition in the bilayer Hubbard model, *Phys. Rev. B* **111**, 245103 (2025).
- [31] Y. Pan, R. Ma, C. Chen, Z. Jia, and T. Ma, Competition between d-wave and  $d+is$ -wave superconductivity in the Hubbard model on a checkerboard lattice, *Phys. Rev. B* **110**, 144509 (2024).
- [32] A. Bohrdt, L. Homeier, C. Reinmoser, E. Demler, and F. Grusdt, Exploration of doped quantum magnets with ultracold atoms, *Annals of Physics* **435**, 168651 (2021).
- [33] J. Samland, N. Wurz, M. Gall, and M. Köhl, Thermodynamics and density fluctuations in a bilayer Hubbard system of ultracold atoms (2024), [arXiv:2407.11863](https://arxiv.org/abs/2407.11863).

- [34] R. Erik, V. P. Singh, B. Abel, E. Chang, M. Ludwig, J. F. Christopher, and S. Sunami, Observation of a bilayer superfluid with interlayer coherence, *Nature Communications*, **7201** (2025).
- [35] S. A. Kivelson, Making high  $T_c$  higher: a theoretical proposal, *Physica B: Condensed Matter* **318**, 61 (2002).
- [36] E. Berg, D. Orgad, and S. A. Kivelson, Route to high-temperature superconductivity in composite systems, *Phys. Rev. B* **78**, 094509 (2008).
- [37] S. Okamoto and T. A. Maier, Enhanced Superconductivity in Superlattices of High- $T_c$  Cuprates, *Phys. Rev. Lett.* **101**, 156401 (2008).
- [38] R. A. Fontenele, N. C. Costa, T. Paiva, and R. R. dos Santos, Increasing superconducting  $T_c$  by layering in the attractive Hubbard model, *Phys. Rev. A* **110**, 053315 (2024).
- [39] P. M. Dee, S. Johnston, and T. A. Maier, Enhancing  $T_c$  in a composite superconductor/metal bilayer system: A dynamical cluster approximation study, *Phys. Rev. B* **105**, 214502 (2022).
- [40] Y. Zhang, P. M. Dee, B. Cohen-Stead, T. A. Maier, S. Johnston, and R. Scalettar, Optimizing the critical temperature and superfluid density of a metal-superconductor bilayer, *Phys. Rev. B* **112**, 064510 (2025).
- [41] G. Wachtel, A. Bar-Yaacov, and D. Orgad, Superfluid stiffness renormalization and critical temperature enhancement in a composite superconductor, *Phys. Rev. B* **86**, 134531 (2012).
- [42] T. A. Maier and D. J. Scalapino, Pairfield fluctuations of a 2D Hubbard model, *npj Quantum Materials* **4**, 1 (2019).
- [43] M. H. Hettler, A. N. Tahvildar-Zadeh, M. Jarrell, T. Pruschke, and H. R. Krishnamurthy, Nonlocal dynamical correlations of strongly interacting electron systems, *Phys. Rev. B* **58**, R7475 (1998).
- [44] T. Maier, M. Jarrell, T. Pruschke, and M. H. Hettler, Quantum cluster theories, *Rev. Mod. Phys.* **77**, 1027 (2005).
- [45] U. R. Hähner, G. Alvarez, T. A. Maier, R. Solcà, P. Staar, M. S. Summers, and T. C. Schulthess, DCA++: A software framework to solve correlated electron problems with modern quantum cluster methods, *Computer Physics Communications* **246**, 106709 (2020).
- [46] E. Gull, P. Werner, O. Parcollet, and M. Troyer, Continuous-time auxiliary-field monte carlo for quantum impurity models, *Europhysics Letters* **82**, 57003 (2008).
- [47] T. A. Maier, M. S. Jarrell, and D. J. Scalapino, Structure of the pairing interaction in the two-dimensional Hubbard model, *Phys. Rev. Lett.* **96**, 047005 (2006).
- [48] D. J. Scalapino, *Handbook of High-Temperature Superconductivity: Theory and Experiment* (Springer, New York, NY, 2007) pp. 495–526.
- [49] X. Liu and M. Jiang, Enhanced superconductivity via layer differentiation in trilayer Hubbard model (2025), [arXiv:2507.06614](https://arxiv.org/abs/2507.06614).
- [50] T. A. Maier, M. Jarrell, and D. J. Scalapino, Pairing interaction in the two-dimensional Hubbard model studied with a dynamic cluster quantum Monte Carlo approximation, *Phys. Rev. B* **74**, 094513 (2006).
- [51] G. Homann, M. H. Michael, J. G. Cosme, and L. Mathey, Dissipationless counterflow currents above  $T_c$  in bilayer superconductors, *Phys. Rev. Lett.* **132**, 6 (2024).
- [52] E. Gull, M. Ferrero, O. Parcollet, A. Georges, and A. J. Millis, Momentum-space anisotropy and pseudogaps: A comparative cluster dynamical mean-field analysis of the doping-driven metal-insulator transition in the two-dimensional hubbard model, *Phys. Rev. B* **82**, 155101 (2010).
- [53] W. Wu, M. S. Scheurer, S. Chatterjee, S. Sachdev, A. Georges, and M. Ferrero, Pseudogap and Fermi-Surface Topology in the Two-Dimensional Hubbard Model, *Phys. Rev. X* **8**, 021048 (2018).
- [54] H. Lee, Y.-Z. Zhang, H. O. Jeschke, and R. Valentí, Competition between band and mott insulators in the bilayer hubbard model: A dynamical cluster approximation study, *Phys. Rev. B* **89**, 035139 (2014).